



Transformation pathway and toxic intermediates inhibition of photocatalytic NO removal on designed Bi metal@defective $\text{Bi}_2\text{O}_2\text{SiO}_3$



Xinwei Li^a, Wendong Zhang^b, Jieyuan Li^{a,c}, Guangming Jiang^a, Ying Zhou^d, ShunCheng Lee^e, Fan Dong^{a,d,*}

^a Chongqing Key Laboratory of Catalysis and New Environmental Materials, College of Environment and Resources, Chongqing Technology and Business University, Chongqing, 400067, China

^b Chongqing Key Laboratory of Inorganic Functional Materials, Department of Scientific Research Management, Chongqing Normal University, Chongqing, 401331, China

^c College of Architecture and Environment, Institute of New Energy and Low Carbon Technology, Sichuan University, Sichuan, 610065, China

^d The Center of New Energy Materials and Technology, School of Materials Science and Engineering, Southwest Petroleum University, Chengdu, 610500, China

^e Department of Civil and Environmental Engineering, The Hong Kong Polytechnic University, Hong Kong, China

ARTICLE INFO

Keywords:

Bi metal
Oxygen vacancy
Photocatalysis
Toxic intermediates inhibition
In situ DRIFTS

ABSTRACT

The design of highly efficient visible-light photocatalysts and the elucidation of decomposition mechanisms are the two key tasks in environmental remediation. Herein, we utilized theoretical calculations to design a Bi metal-based visible-light photocatalyst ($\text{Bi}@\text{BiOSi}$) with surface plasmon resonance (SPR) properties, showing that the unique electron delivery channel was formed at the Bi metal/ $\text{Bi}_2\text{O}_2\text{SiO}_3$ interface. The $\text{Bi}@\text{BiOSi}$ nanosheets were used for photocatalytic removal of ppb-level atmospheric NO, with Bi metal-based SPR resulting in enhanced visible light capture and charge separation efficiency, whereas oxygen vacancy induced the formation of a midgap level and promoted O_2 activation. As a result, generation of superoxide and hydroxyl radicals over $\text{Bi}@\text{BiOSi}$ was promoted, favoring photocatalytic NO removal. To elucidate the reaction mechanism, the products distribution during adsorption and photocatalytic NO oxidation on $\text{Bi}@\text{BiOSi}$ were determined by in situ DRIFTS, which revealed that the increased production of reactive species inhibited the toxic intermediates (N_2O_4) formation and increased the selectivity of the NO-to- NO_3^- transformation via the synergy of oxygen vacancy and Bi metal. Thus, this work provides new insights into the design of non-noble metal-based photocatalysts and establishes a novel method of inhibiting the toxic intermediates production in photocatalysis for efficient and safe air purification.

1. Introduction

NO is one of the major air pollutants emitted by vehicles and power plants [1–3], being a typical PM_{2.5} precursor and playing an important role in the formation of haze and photochemical smog [4,5]. Generally, chemical removal of NO is mainly achieved using conventional approaches such as selective catalytic reduction [6], three-way catalysis [7], wet scrubbing [8], biofiltration [9], and oxidation-adsorption processes [10]. However, all these processes are generally developed for the removal of high-concentration NO from industrial emissions, being not economically suitable for use in urban atmospheric environments, which are characterized by NO concentration of parts per billion (ppb). However, photocatalysis is regarded as an alternative low-concentration NO removal technology due to its energy saving

potential, low cost, and green easy-to-operate character [11–14].

In general, the reactive radical-mediated photocatalytic oxidation of NO affords nitrate ions adsorbed on the catalyst surface, which are easily washed away [15,16]. However, in certain cases, photocatalytic oxidation is undesirable due to its potential of concomitantly producing toxic intermediates such as NO_2 and N_2O_4 that are released into the atmosphere and subsequently cause secondary pollution [17–19]. Thus, despite being largely ignored, the above issue presents a major challenge for the application of photocatalysis in air purification.

Although noble metal (Pt, Pd, Au)-based co-catalysts have been reported to inhibit the formation of toxic intermediates during photocatalytic oxidation of aqueous contaminants [20–22], their widespread application is hindered by high cost. Moreover, the complicated mechanism of photocatalytic NO oxidation in air remains incompletely

* Corresponding author at: Chongqing Key Laboratory of Catalysis and New Environmental Materials, College of Environment and Resources, Chongqing Technology and Business University, Chongqing, 400067, China.

E-mail address: dfctbu@126.com (F. Dong).

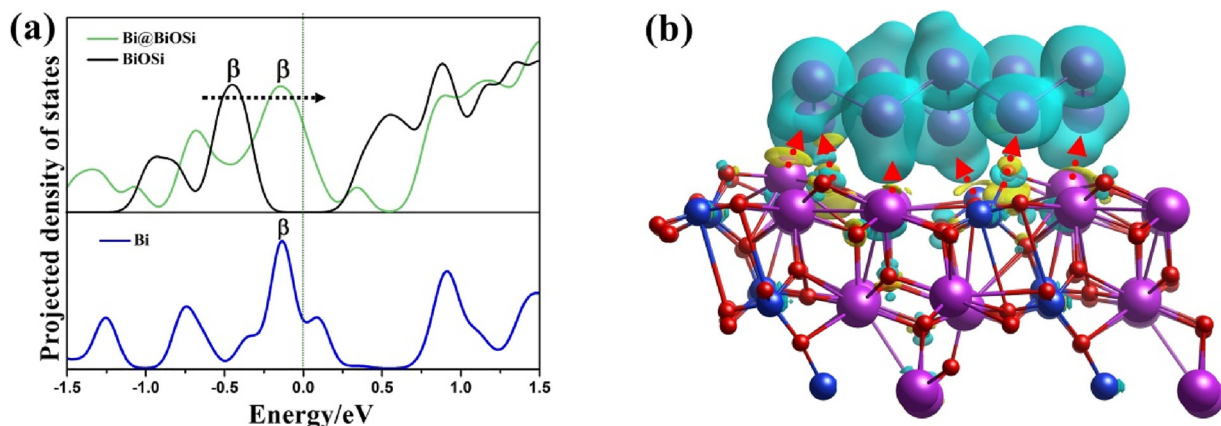


Fig. 1. Projected density of states (PDOS) of Bi atom, BiOSi and Bi@BiOSi (a). The charge difference between each atom in Bi@BiOSi structure (b). Purple, red and blue spheres depict Bi, O and Si atoms. Charge-accumulation and charge-depletion regions are shown in blue and yellow, respectively. (For interpretation of the references to colour in this figure legend, the reader is referred to the web version of this article).

understood. Recently, Dong et al. found that Bi, a non-noble metal, demonstrates direct plasmonic photocatalytic performance [23], which allows it to be used as a noble metal substitute to improve the photocatalytic performance of other semiconductors [24–27]. Thus, the fabrication of a Bi metal-based model photocatalyst should contribute to our detailed understanding of the NO removal mechanism, particularly to that of toxic intermediate generation, an important issue that has been largely overlooked. This could help to establish effective approaches of inhibiting the formation of such intermediates during photocatalytic NO oxidation.

Herein, we designed and fabricated Bi metal@ $\text{Bi}_2\text{O}_2\text{SiO}_3$ (Bi@BiOSi) as a model catalyst, utilizing density functional theory (DFT) calculations to predict the optimized electronic structure of Bi@BiOSi and the mechanism of charge transfer between its constituents. Based on DFT insights, Bi@BiOSi composites were fabricated via a facile chemical reduction method and used for the removal of ppb-level NO in a continuous air flow reactor under visible light illumination, with the obtained results demonstrating the simultaneous deposition of Bi metal and formation of oxygen vacancies (OVs). Moreover, Bi metal with SPR effect and working as electron sink enhanced the visible light capture and charge separation efficiencies, whereas OV generation induced the formation of a midgap level to make Bi@BiOSi catalysts visible light active. At the same time, the coexistence of OVs and Bi metal had synergistic effects on NO and O_2 activation on catalyst. Consequently, the production of both superoxide and hydroxyl radicals on Bi@BiOSi was significantly enhanced, leading to much more efficient photocatalytic NO removal under visible light irradiation. Most importantly, the adsorption and photocatalytic oxidation of NO on Bi@BiOSi were investigated by *in situ* DRIFTS, which revealed that the enhanced production of reactive species inhibited the generation of toxic intermediates (N_2O_4) and increased the selectivity of the NO-to- NO_3^- conversion.

2. Experimental

Details of catalyst preparation, Characterization method and theoretical calculation methods are given in Supporting Information.

2.1. Evaluation of visible light photocatalytic activity

The photocatalytic activities of as-prepared samples were evaluated by removal of ppb-level NO in a continuous flow reactor under visible light irradiation, with detailed procedures presented in the Supporting Information (Fig. S1).

2.2. *In situ* DRIFTS investigation of the photocatalytic NO oxidation mechanism

In situ DRIFTS measurements (Fig. S3) were conducted using a TENSOR II Fourier transform infrared (FT-IR) spectrometer (Bruker) equipped with an *in situ* diffuse reflectance cell (Harrick) and a high-temperature reaction chamber (HVC), which featured two gas ports and two cooling ports. High-purity He, high-purity O_2 , and 100 ppm NO in He were fed into the reaction system, and a three-way ball valve was used for switching between target (NO) and purge (He) gases. The total gas flow rate equaled 100 mL/min, and the concentration of NO was controlled at 50 ppm by dilution with O_2 . The chamber was enclosed within a dome with three windows: two IR light-transparent ZnSe windows and one UV light-transparent quartz window for photocatalyst illumination. A Xe lamp (MVL-210, Optpe, Japan) (Fig. S3e) was used as the light source.

3. Results and discussion

3.1. Theoretical design of the Bi@BiOSi model catalyst

The BiOSi catalyst comprised $[\text{Bi}_2\text{O}_2]^{2+}$ slabs sandwiched between SiO_3^{2-} pyroxene file layers [28,29]. In the first step, we modeled and optimized the electronic configuration of Bi@BiOSi, which typically featured exposed (311) facets with one Bi particle layer homogeneously deposited on the above facet (Fig. S4) [30]. The effect of top Bi metal could be well understood by employing the projected density of states (Fig. 1a). Notably, the positive shift of the Bi β peak of Bi@BiOSi relative to that of pristine BiOSi indicated that Bi atoms in Bi@BiOSi possessed a higher electron distribution. The corresponding partial decomposed charge densities further confirmed that it is the top Bi layer carrying more charge (Fig. S5). Then, the electron localization functional shown in Fig. S6 illustrates the existence of a covalent interaction between top Bi layer and substrate BiOSi (311), whereas the charge difference distribution (Fig. 1b) reveals that random electrons would migrate from BiOSi to the top Bi layer causing charge accumulation over top Bi atoms. The number of top Bi atoms did not affect the charge transfer direction (Fig. S7). Further, the electrostatic potential of Bi@BiOSi configuration presented in Fig. S8 implies that Bi metal lower the electron transfer energy due to working as an electron sink to ensure the directional movement of electrons from BiOSi to top Bi metal. Hence, the Bi@BiOSi configuration would originally improve the charge transport at the interface by Bi metal incessantly attracting charge transfer.

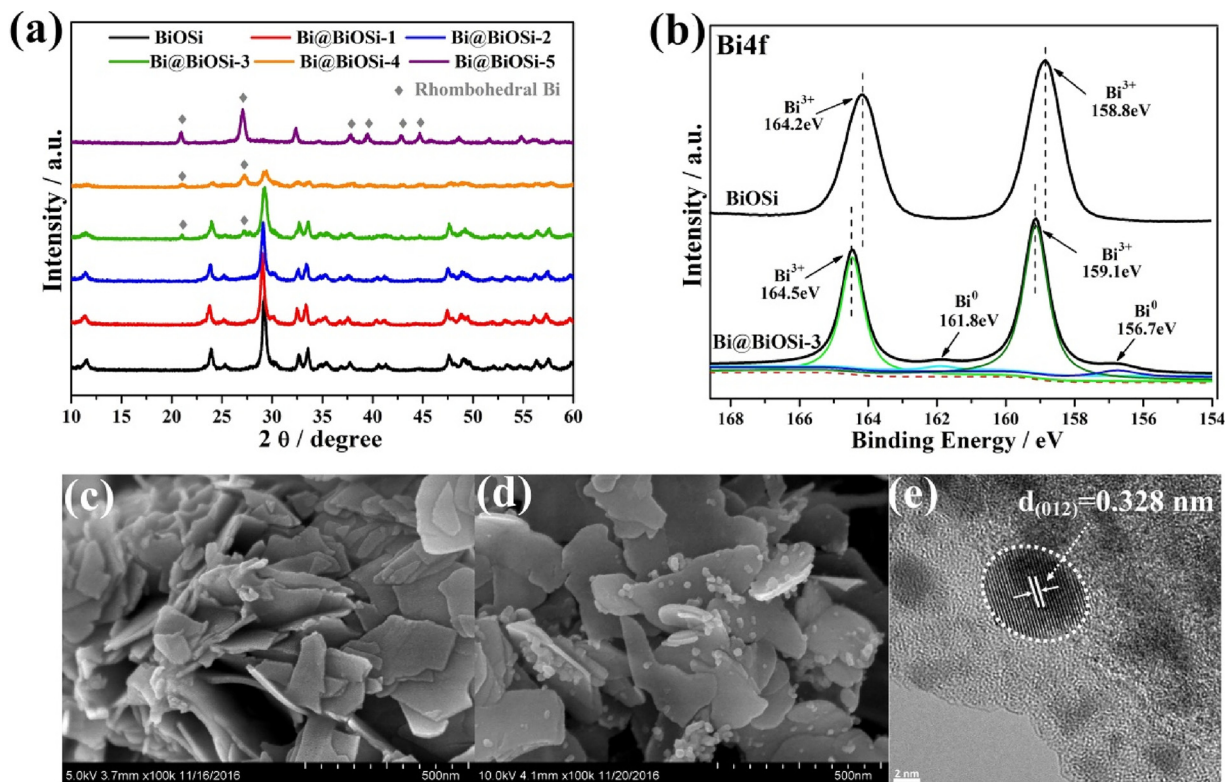


Fig. 2. XRD patterns of BiOSi and Bi@BiOSi samples (a), XPS spectra of Bi4f in BiOSi and Bi@BiOSi-3 (b), SEM images of BiOSi (c) and Bi@BiOSi-3 (d), HRTEM image of Bi@BiOSi-3 (e).

3.2. Synthesis and structure of Bi@BiOSi

Since the deposition of Bi metal on BiOSi could promote the separation and transfer of charges as key photocatalysis steps, we used NaBH₄ as a reducing agent to achieve Bi metal deposition on the surface of BiOSi. The X-ray diffraction (XRD) patterns of as-prepared samples (Fig. 2a) showed that the diffraction peaks of BiOSi were well matched with the orthorhombic phase of Bi₂O₂SiO₃ (PDF#75-1483) [31], with their intensity decreasing with increasing NaBH₄ concentration. Moreover, a new phase, namely rhombohedral Bi metal (PDF#85-1330) was observed in Bi@BiOSi-3 and Bi@BiOSi-4, with its peak becoming dominant in Bi@BiOSi-5 and thus implying the complete reduction of Bi³⁺ in BiOSi to Bi metal. Similar to XRD analysis, all FT-IR spectra (Fig. S9) relevant characteristic peaks were disordered in the spectra of Bi@BiOSi-4, being totally absent in those of Bi@BiOSi-5.

Fig. 2b shows the XPS spectra of Bi4f, where the two peaks located at 164.2 and 158.8 eV for BiOSi sample are attributed to Bi4f_{7/2} and Bi4f_{5/2} peaks of Bi³⁺ respectively [12,32]. In contrast, there are two additional peaks at 161.8 and 156.7 eV assigned to Bi⁰ in Bi@BiOSi-3 [33]. Moreover, Bi 4f (Fig. 2b) and O 1 s (Fig. S10c) peaks of Bi@BiOSi-3 had higher binding energies than those of pristine BiOSi, suggesting the existence of a covalent interaction between Bi metal and BiOSi, in agreement with theoretical calculations [34,35]. The atomic content of Bi³⁺, Bi⁰, Si and O elements and the ratio of Bi metal to Bi₂O₂SiO₃ of the samples are given in Table S1. Considering that Bi metal is in situ introduced on the surface of BiOSi, the interfacial contact between BiOSi and Bi is intimate, promoting interfacial charge transfer.

Scanning electron microscopy (SEM) and transmission electron microscopy (TEM) were employed for morphological characterization, revealing that pure BiOSi comprised interconnected ultrathin nanosheets (Figs. 2c, S11a, b and S12a, b). Correspondingly, small nanoparticles uniformly distributed on nanosheets were observed for Bi@BiOSi-3 (Figs. 2d, S11c, d and S12c, d). Representative high-resolution TEM (HRTEM) images of BiOSi and Bi@BiOSi-3 (Fig. S13a, b and c, d,

respectively) revealed that in situ formed Bi nanoparticles with mean particle size of 4.0 nm (Fig. S14) were dispersed on the surface of BiOSi nanosheets. The BET surface area of Bi@BiOSi samples are 27.2, 29.0, 29.8, 26.3, 28.8 m²/g, respectively, all higher than that of bulk BiOSi (19.7 m²/g). With more nanoparticle metal Bi deposited on the surface, the BET surface areas are increased. N₂ adsorption-desorption isotherm and pore diameter distributions of samples are given in Fig. S15. Moreover, the lattice spacing of 0.328 nm (Fig. 2e) identified in the nanoparticle region (circled part) was well matched with the (012) plane of rhombohedral Bi.

3.3. Visible light photocatalytic NO removal

The as-prepared catalysts were used for photocatalytic NO removal under visible light illumination in a continuous air flow reactor, with the obtained results (Fig. 3a) showing that pristine BiOSi exhibited negligible visible light activity. However, Bi metal deposition significantly improved the photocatalytic activity, with the highest NO removal efficiency of 50.2% observed for Bi@BiOSi-3 being followed by those of Bi@BiOSi-2 (38.6%), Bi@BiOSi-4 (27.7%), Bi@BiOSi-1 (14.2%), and Bi@BiOSi-5 (13.8%). The corresponding NO₂ generations are given in Fig. S16. Nevertheless, the excessive amounts of Bi metal in Bi@BiOSi-4 and Bi@BiOSi-5 were expected to negatively affect photocatalytic activity. Notably, Bi@BiOSi-3 exhibits superior photocatalytic activity in comparison with common photocatalysts P25 and g-C₃N₄ (Fig. S17).

After the photocatalytic activity test, the final products NO₂⁻ and NO₃⁻ on the catalysts surface were washed with 100 mL deionized water and determined by ion chromatography (IC) (Fig. S18). The NO₂⁻ and NO₃⁻ are the final products of photocatalytic NO oxidation. The concentration of NO₂⁻ and NO₃⁻ accumulated on different catalyst is consistent with the photocatalytic activity, i.e. the most efficient Bi@BiOSi-3 generated maximum amount of NO₃⁻ product on the catalyst surface. The durability of Bi@BiOSi-3 was further tested for five

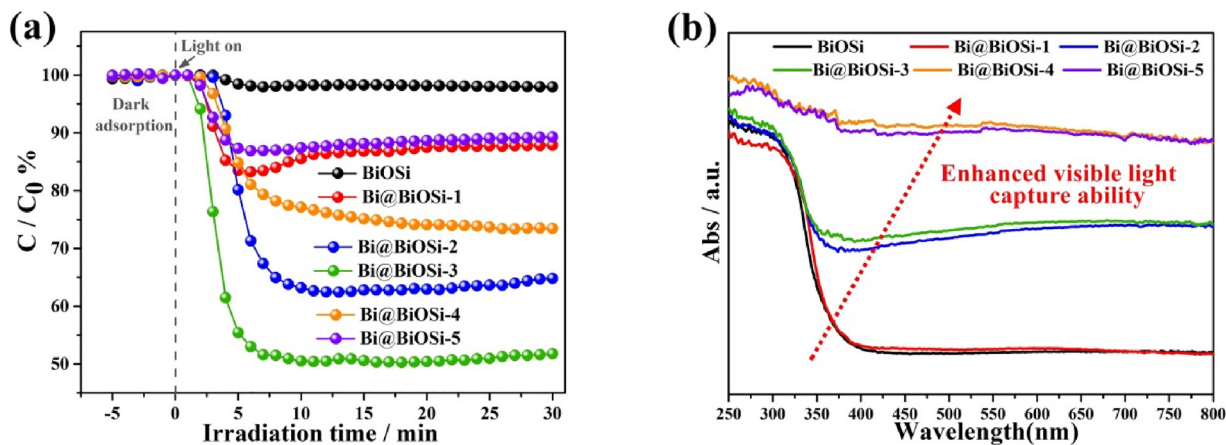


Fig. 3. Visible light photocatalytic performances (a) and the UV–vis diffuse reflectance spectra of BiOSi and Bi@BiOSi samples (b).

repeated irradiations (Fig. S19a), which implies that the Bi@BiOSi was photo-chemically stable with little deactivation. Catalyst XRD and XPS comparison after repeated experiments are also given in Fig. S19b–d

3.4. Optical properties and band structure

Since Bi metal exhibits visible light-induced surface plasmon resonance (SPR) effect [36], Bi@BiOSi samples showed enhanced visible light capture ability (Fig. 3b). In these samples, Bi metal could concentrate incident photon energy into plasmon oscillations and thus significantly enhanced the electromagnetic field (simulated by FDTD techniques in Fig. S20) to facilitate the separation of electrons (e^-) and holes (h^+) [37–39]. The characteristic PL peaks of Bi@BiOSi (Fig. S21) were significantly less intense than those of BiOSi, further implying that the introduction of Bi metal inhibited charge carrier recombination.

Plots of $(ah\nu)^{1/2}$ versus photon energy and the valence-band XPS spectra of BiOSi and Bi@BiOSi-3 (Fig. S22) showed that Bi metal introduction did not significantly affect the band gap energy and the valence band position [40,41]. Since the conduction band edge of Bi@BiOSi-3 (-1.03 eV) was more negative than that of the Fermi level of Bi metal (-0.17 eV) [23], the BiOSi-to-Bi flow of photoexcited electrons in Bi@BiOSi-3 was thermodynamically favorable. However, the band gap of BiOSi is 3.2 eV (Fig. S22a), which can be hardly excited under visible light irradiation.

The solid-state electron paramagnetic resonance (EPR) is employed to investigate the nature of defects under room temperature [42]. There are little OVs in BiOSi as the EPR signal in dark is negligible (Fig. 4a). However, the Bi@BiOSi samples show gradually enhanced EPR signal with the increase amount of Bi metal at $g = 2.004$, implying that an increased amount of OVs was generated [41]. Also, these EPR signals are found to be intensified under visible light irradiation, further confirming that the charge mobility of Bi@BiOSi samples can be effectively promoted for Bi metal [43–45]. More importantly, OVs would induce the formation of an intermediate level, as revealed by DFT calculations (Fig. S23), allowing photo-electron excited from the valence band to the intermediate level and then to the conduction band to induce following reactions (Fig. S24) [46].

3.5. Reactants activation

The adsorption of O_2 and NO on the catalyst surface is a key step in gas-solid photocatalytic reaction. Firstly, O_2 activation is a quite essential step by producing active free radicals that directly work on contaminants. Also, O_2 activation could trap electrons thus effectively prevent carrier recombination. Therefore, the most stable O_2 adsorption results (Fig. S25) after optimizing the initial configurations are obtained to get access to the effect of OVs and Bi metal for O_2 activation.

Apparently, O–O bond length is enlarged on both OV-BiOSi and Bi-BiOSi configurations. Moreover, the energy of O_2 molecule adsorption (E_{ads}) in the four structures are: OV-BiOSi (-2.29 eV) < side-Bi-BiOSi (-1.84 eV) < BiOSi (-1.61 eV) < top-Bi-BiOSi (-1.41 eV). These results suggest that side-Bi-BiOSi configuration would facilitate O_2 activation to certain extent while OV-BiOSi is the most beneficial configuration for O_2 adsorption and activation for its most negative E_{ads} and largely lengthened O–O bond. Normally, surface OVs could supply coordinately unsaturated sites for O_2 adsorption and activation and thus promote superoxide radical ($\cdot O_2^-$) formation [47]. Consequently, enhanced ESR signals of DMPO- $\cdot O_2^-$ (Fig. 4b) could be observed for Bi@BiOSi-3 compared with pristine BiOSi. Additionally, the enhanced ESR signals of hydroxyl radicals ($\cdot OH$) (Fig. S26) can be ascribed to increased charge separation efficiency.^{12, 29} The observed $\cdot OH$ were formed via the oxidation of surface OH^- by photogenerated h^+ , since the potential energy of valence-band h^+ (2.05 eV) was higher than that of $OH^-/\cdot OH$ (1.99 eV) [12,48]. Thus, the increased production of highly oxidizing active radicals favored the complete oxidation of NO.

In addition, NO adsorption over the four configurations was calculated as shown in Fig. S27. The side-Bi-BiOSi is the most favorable configuration for NO adsorption as indicated by the most negative adsorption energy and largely lengthened N–O bond. According to the total charge calculated by Bader method [49], Bi metal could facilitate the NO by accepting electrons, while the OVs promote NO activation by donating electrons.

In the actual reaction situation, the O_2 and NO coexist on the catalyst surface. Therefore, we discussed the NO and O_2 co-adsorption on OV-BiOSi and side-Bi-BiOSi structure that either in favors of O_2 adsorption or NO adsorption. In the presence of OVs (Fig. 4c), O_2 is preferentially adsorbed and activated for its largely lengthened O–O bond. While the adsorption of NO seems to be limited when coexisting with O_2 for its shorten N–O bond. Also the density difference result shows that the random electrons are accumulated on O_2 for its activation in priority.

For side-Bi-BiOSi structure (Fig. 4d), it could be seen that the NO is prior to receive electrons from Bi metal then transfer them to O_2 for its activation. Also, Bi metal would not prevent O_2 from adsorption while promoting NO adsorption in side-Bi-BiOSi structure according to N–O and O–O bond length variation. Interestingly, the total charge of NO in the two structures remains unchanged, including the electron loss in OV-BiOSi and charge accumulation in side-Bi-BiOSi. The as-prepared catalyst is largely influenced by OVs and Bi metal. That is to say, it is favorable for O_2 activation on OVs dominated area, whereas the NO adsorption would be promoted by Bi metal.

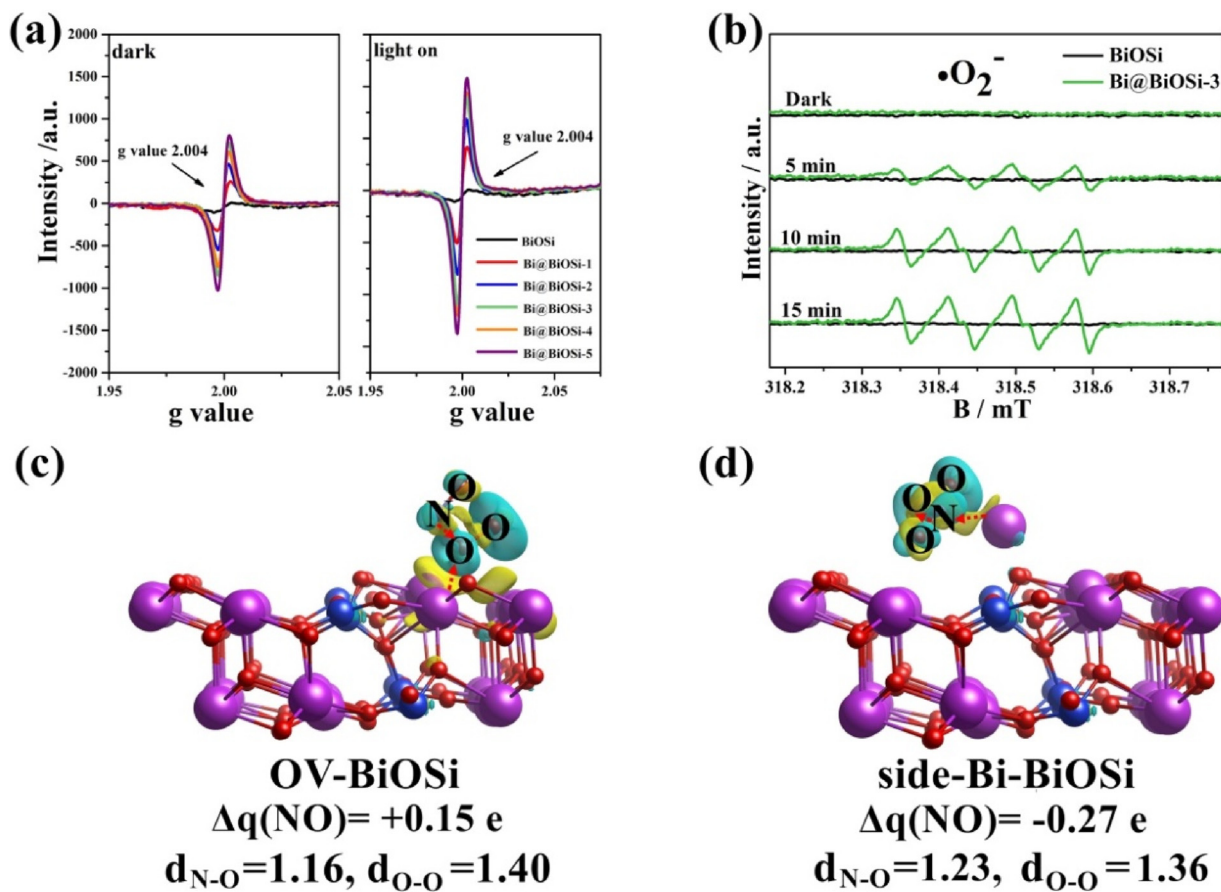


Fig. 4. Solid-state EPR spectra of BiOSi and Bi@BiOSi samples (a). DMPO ESR spectra of $\cdot\text{O}_2^-$ in methanolic dispersions in the dark and under visible light irradiation ($\lambda \geq 420 \text{ nm}$) (b). NO and O₂ coadsorption in BiOSi (c) and side-Bi-BiOSi (d) configuration. All lengths are given in Å, with the colour coding of atoms matching that of Fig. 1.

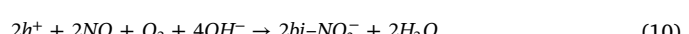
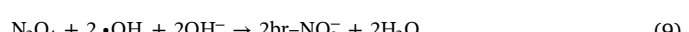
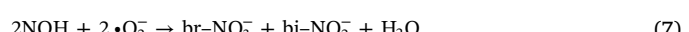
3.6. Mechanism of photocatalytic NO oxidation and toxic intermediates inhibition

The mechanism of photocatalytic NO oxidation was probed by in situ DRIFTS to directly monitor NO and O₂ adsorption and reactions on the catalyst surface. In situ DRIFT spectra recorded during adsorption and photocatalytic reaction on BiOSi and Bi@BiOSi samples as shown in Fig. S28 and Fig. 5. NO and O₂ led to the formation of several adsorbed NO_x species with adsorption bands attribution shown in Table S3.

During adsorption (Fig. S28), NO (1715–1724 cm⁻¹) is capable of simultaneously reacting with surface hydroxyl groups (broad 3300 cm⁻¹) to form NOH (around 1100 cm⁻¹) and bi-NO₂⁻ (1590, 1594 cm⁻¹) (Eq. (1)) with quite low content [50–53]. Also, NO together with O₂ is more likely to convert into N₂O₄ (1376–1350 cm⁻¹) [54], the dipolymer of NO₂, that is an undesirable toxic intermediates (Eq. (2)). However, NO may react with neighboring O₂ present at the OVs (O₂²⁻) to afford surface-adsorbed c-NO₂⁻ and m-NO₃⁻ (Eq. (3)) to prevent N₂O₄ generation [48]. That is to say, gradually generated OVs in Bi@BiOSi samples are able to inhibit the conversion of NO into N₂O₄ during the adsorption period to some extent.

After photocatalytic reaction sparked, $\cdot\text{O}_2^-$ and $\cdot\text{OH}$ radicals would be produced via photoexcited h⁺ and e⁻ reacted with surface O₂ and OH⁻, respectively (Eqs. (4)–(6)), being subsequently utilized for the oxidation of NOH and N₂O₄ to bi-NO₂⁻ and br-NO₃⁻ (1695 cm⁻¹) thoroughly (Eqs. (7)–(9)) [53]. That is to say, sufficient generated active radicals are able to oxidize all intermediates completely avoiding toxic intermediates accumulation effectively. Moreover, photoexcited h⁺ could also directly oxidize NO to bi-NO₃⁻ (1404 cm⁻¹) (Eq. (10))

[52,55]. The overall process of NO adsorption and photocatalytic oxidation in Bi@BiOSi sample is given in Fig. S29. Control experiments on DRIFT spectra over P25, CN and without photocatalyst are given in Fig. S30. There is no detectable IR peak under both dark and light on situation, without photocatalyst which means NO would not be removed without photocatalytic reaction. On the other hand, NO⁺, NO, N₂O₄, NO₂⁻ and NO₃⁻ are detected over CN and P25 under light irradiation, which are common photocatalytic NO oxidation intermediates and final products [56–58].



The normalization method was used to figure out the intermediates difference during adsorption and reaction stage (Fig. 6). The content percentage means the one single species as a percentage of total NO_x

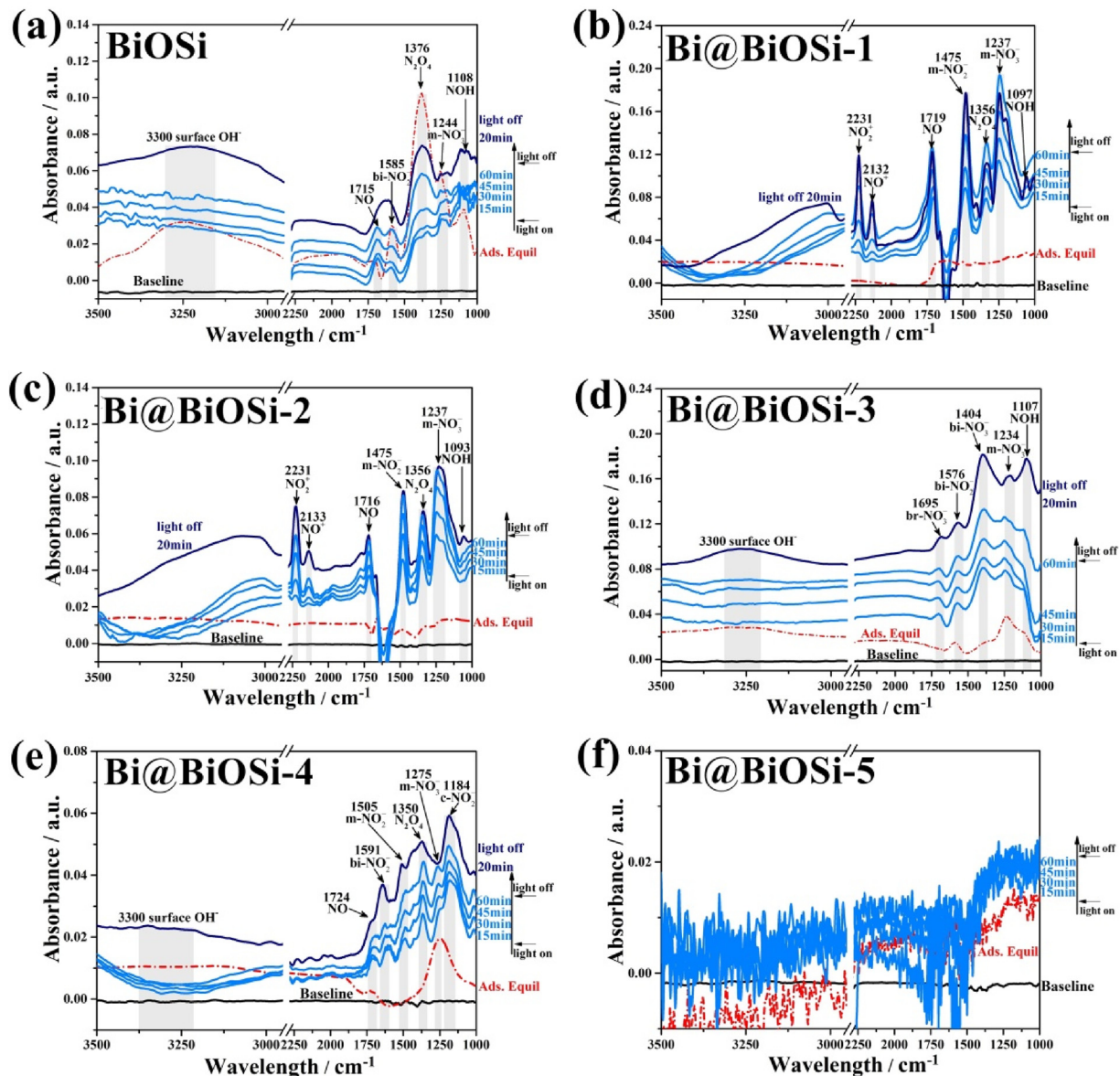


Fig. 5. In situ DRIFT spectra recorded during NO photocatalytic reaction over BiOSi (a) and Bi@BiOSi samples (b–f).

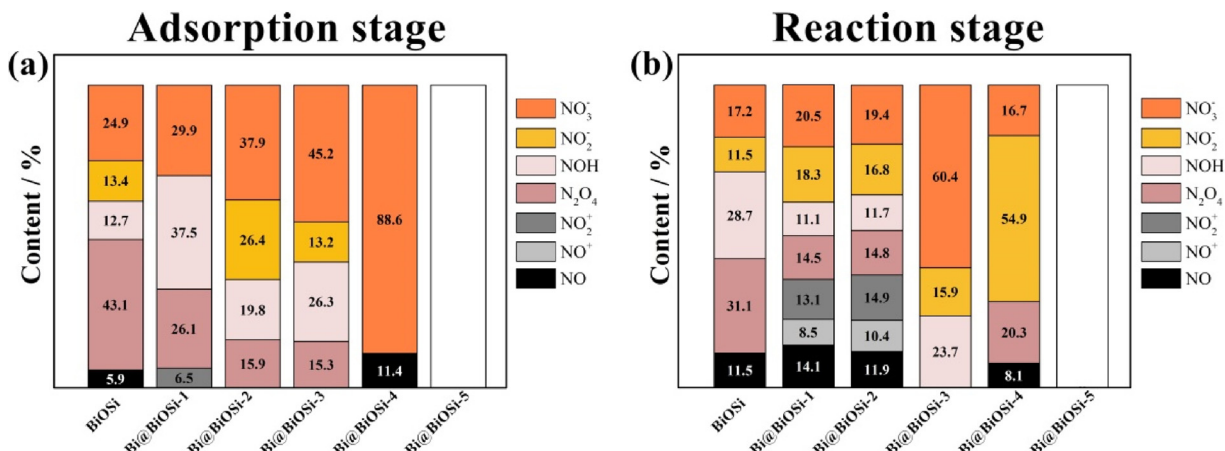


Fig. 6. Normalized the reaction intermediates and final products on each sample after the adsorption stage (a) and photocatalytic reaction stage (b).

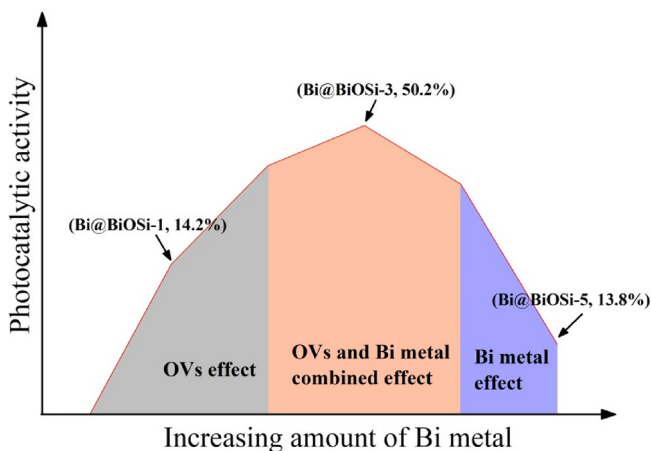


Fig. 7. Schematic illustration of the synergistic effects of OVs and Bi metal on the photocatalytic activity.

intermediates species of each sample after adsorption and reaction stage.

From the product percentage shown in Fig. 6a, the main product on BiOSi during dark adsorption is N_2O_4 . Also, the yield of N_2O_4 is highest in BiOSi among all samples in adsorption stage. However, the generation of N_2O_4 in this stage is decreased from Bi@BiOSi-1 to Bi@BiOSi-4 sample with gradual increased OVs and Bi metal, which means the generation of N_2O_4 is suppressed in the adsorption phase. As for Bi@BiOSi-5 samples, no characteristic peaks can be detected.

For the photocatalytic reaction stage, certain content of NO^+ and NO_2^+ can be detected in Bi@BiOSi-1 and Bi@BiOSi-2 samples as shown in Fig. 6b [49]. That is to say, the NO and NO_2 tend to lose electrons in Bi@BiOSi-1 and Bi@BiOSi-2 samples. In combination with DFT, the OVs play a main role in these two samples as NO is more like to be electron donor. Nevertheless, NO^+ and NO_2^+ are not detected in Bi@BiOSi-3 and Bi@BiOSi-4 with increased amount of Bi metal which is prone to donate electrons to the adsorbed NO. It is worth noting that the generation of final products NO_2^- and NO_3^- reaches to the highest level in Bi@BiOSi-3 samples during photocatalysis reaction, which is accounted for its most positive response in NO removal. The selectivity of the NO-to- NO_3^- transformation during photocatalysis could be improved largely with combined effect of OVs and Bi metal. There is still no any peak being detected in Bi@BiOSi-5 samples after light on, which

indicates that the excessive Bi metal is wrapped on the surface of the catalyst, which would prevent NO from adsorption on the catalyst surface (Fig. S27).

In general, the photocatalytic NO removal would reach maximum when the content of OVs and Bi metal is optimized. The “volcano-like” variation of the photocatalytic activity of Bi@BiOSi samples should be ascribed to the synergy of OVs and Bi metal, which can be schemed in Fig. 7.

Thus, Bi@BiOSi is an outstanding photocatalyst for efficient and safe air purification. The detailed photocatalytic reaction mechanism is illustrated in Fig. 8.

4. Conclusion

Although only a model Bi@BiOSi catalyst is described herein, this study has significant implications for modification of the abundant Bi-containing semiconductors. Bi metal was shown to increase the visible light absorption and carrier transportation efficiency of the studied photocatalyst due to exhibiting SPR properties and working as electron sink. Meanwhile, the simultaneously generated OVs form an intermediate energy level, making it possible for the wide band gap semiconductor being responded to visible light. Moreover, the co-existed OVs and Bi metal were demonstrated to have synergy effect on reactants activation on the catalyst surface. These parameters are decisive factors for sufficient active radical generation during photocatalysis. Then, the generation of N_2O_4 was effectively inhibited during adsorption as well as reaction process by the largely produced active radicals via in situ DRIFTS monitoring. Finally, the high selectivity of the NO-to- NO_3^- transformation is accomplished by the synergy of OVs and Bi metal. The above insights should enable the modification of other Bi-containing semiconductors to highly inhibit the generation of toxic intermediates, an important issue that has been largely overlooked.

Acknowledgements

This work was supported by the National Natural Science Foundation of China (21822601, 21777011, and 21501016), the National R&D Program of China (2016YFC0204702), the Innovative Research Team of Chongqing (CXTDG201602014), the Natural Science Foundation of Chongqing (cstc2017jcyjBX0052), and the Plan for "National Youth Talents" of the Organization Department of the Central Committee. The authors also acknowledge AM-HPC in Suzhou, China

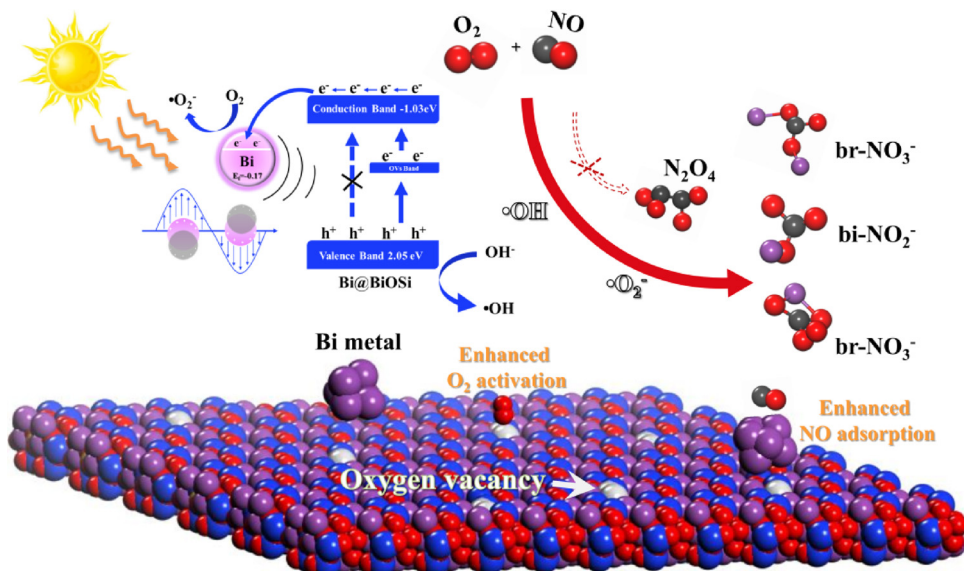


Fig. 8. Scheme of processes occurring during visible-light-driven photocatalytic NO removal on Bi@BiOSi-3.

for computational support.

Appendix A. Supplementary data

Supplementary material related to this article can be found, in the online version, at doi:<https://doi.org/10.1016/j.apcatb.2018.09.032>.

References

- [1] M. Jacobson, W. Colella, D. Golden, Cleaning the air and improving health with hydrogen fuel-cell vehicles, *Science* 308 (2005) 1901–1905.
- [2] J.J. Schauer, M.J. Kleeman, G.R. Cass, B.R.T. Simoneit, Measurement of emissions from air pollution sources. 5. C₁–C₃₂ organic compounds from gasoline-powered motor vehicles, *Environ. Sci. Technol.* 36 (2002) 1169–1180.
- [3] H. Wang, W. He, X. Dong, H. Wang, F. Dong, In situ FT-IR investigation on the reaction mechanism of visible light photocatalytic NO oxidation with defective g-C₃N₄, *Sci. Bull.* 63 (2018) 117–125.
- [4] X. Querol, A. Alastuey, S. Rodriguez, F. Plana, C.R. Ruiz, N. Cots, G. Massagué, O. Puig, PM10 and PM2.5 source apportionment in the Barcelona metropolitan area, Catalonia, Spain, *Atmos. Environ.* 35 (2001) 6407–6419.
- [5] X. Wang, J. Chen, T. Cheng, R. Zhang, X. Wang, Particle number concentration, size distribution and chemical composition during haze and photochemical smog episodes in Shanghai, *J. Environ. Sci.* 26 (2014) 1894–1902.
- [6] M. Casapu, O. Kröcher, M. Elsener, Screening of doped MnO_x–CeO₂ catalysts for low-temperature NO-SCR, *Appl. Catal. B: Environ.* 88 (2009) 413–419.
- [7] T. Kobayashi, T. Yamada, K. Kayano, Effect of basic metal additives on NO_x reduction property of Pd-based three-way catalyst, *Appl. Catal. B: Environ.* 30 (2001) 287–292.
- [8] J. Wei, Y. Luo, P. Yu, B. Cai, H. Tan, Removal of NO from flue gas by wet scrubbing with NaClO₂/(NH₄)₂CO solutions, *J. Ind. Eng. Chem.* 15 (2009) 16–22.
- [9] S.P.P. Ottengraf, Biological systems for waste gas elimination, *Trends Biotechnol.* 5 (1987) 132–136.
- [10] A. Ishihara, D. Wang, F. Dumeignil, H. Amano, E.W. Qian, T. Kabe, Oxidative desulfurization and denitrogenation of a light gas oil using an oxidation/adsorption continuous flow process, *Appl. Catal. A: Gen.* 279 (2005) 279–287.
- [11] H. Wang, Y. Sun, G. Jiang, Y. Zhang, H. Huang, Z. Wu, S.C. Lee, F. Dong, Unraveling the mechanisms of visible light photocatalytic NO purification on earth-abundant insulator-based core-shell heterojunctions, *Environ. Sci. Technol.* 52 (2018) 1479–1487.
- [12] Z. Ai, W. Ho, S. Lee, L. Zhang, Efficient photocatalytic removal of NO in indoor air with hierarchical bismuth oxybromide nanoplate microspheres under visible light, *Environ. Sci. Technol.* 43 (2009) 4143–4150.
- [13] Y. Lu, Y. Huang, Y. Zhang, J.J. Cao, H. Li, C. Bian, S.C. Lee, Oxygen vacancy engineering of Bi₂O₃/Bi₂O₂CO₃ heterojunctions: implications of the interfacial charge transfer, NO adsorption and removal, *Appl. Catal. B: Environ.* 231 (2018) 357–367.
- [14] Q. Zhang, Y. Huang, S. Peng, Y. Zhang, Z. Shen, J.J. Cao, W. Ho, S.C. Lee, D.Y. Pui, Perovskite LaFeO₃–SrTiO₃ composite for synergistically enhanced NO removal under visible light excitation, *Appl. Catal. B: Environ.* 204 (2017) 346–357.
- [15] F. Dong, Z. Wang, Y. Li, W.-K. Ho, S.C. Lee, Immobilization of polymeric g-C₃N₄ on structured ceramic foam for efficient visible light photocatalytic air purification with real indoor illumination, *Environ. Sci. Technol.* 48 (2014) 10345–10353.
- [16] W. Cui, J. Li, Y. Sun, H. Wang, G. Jiang, S.C. Lee, F. Dong, Enhancing ROS generation and suppressing toxic intermediate production in photocatalytic NO oxidation on O/Ba co-functionalized amorphous carbon nitride, *Appl. Catal. B: Environ.* 237 (2018) 938–946.
- [17] Y. Byun, K.B. Ko, M. Cho, W. Namkung, K. Lee, D.N. Shin, D.J. Koh, Reaction pathways of NO oxidation by sodium chlorite powder, *Environ. Sci. Technol.* 43 (2009) 5054–5059.
- [18] P.E. Morrow, Toxicological data on NO_x: an overview, *J. Toxicol. Environ. Health* 13 (1984) 205–227.
- [19] A.M. Winer, G.M. Breuer, W.P.L. Carter, K.R. Darnall, J.N. Pitts, Effects of ultraviolet spectral distribution on the photochemistry of simulated polluted atmospheres, *Atmos. Environ.* 13 (1979) (1967) 989–998.
- [20] Z. Zheng, B. Huang, X. Qin, X. Zhang, Y. Dai, M.-H. Whangbo, Facile in situ synthesis of visible-light plasmonic photocatalysts M@TiO₂ (M = Au, Pt, Ag) and evaluation of their photocatalytic oxidation of benzene to phenol, *J. Mater. Chem.* 21 (2011) 9079–9087.
- [21] P. Roy, A.P. Periasamy, C.-T. Liang, H.T. Chang, Synthesis of graphene-ZnO-Au nanocomposites for efficient photocatalytic reduction of nitrobenzene, *Environ. Sci. Technol.* 47 (2013) 6688–6695.
- [22] T. Sano, S. Kutsuna, N. Negishi, K. Takeuchi, Effect of Pd-photodeposition over TiO₂ on product selectivity in photocatalytic degradation of vinyl chloride monomer, *J. Mol. Catal. A: Chem.* 189 (2002) 263–270.
- [23] F. Dong, T. Xiong, Y. Sun, Z. Zhao, Y. Zhou, X. Feng, Z. Wu, A semimetal bismuth element as a direct plasmonic photocatalyst, *Chem. Commun.* 50 (2014) 10386–10389.
- [24] J. Gong, A. Imbault, R. Farnood, The promoting role of bismuth for the enhanced photocatalytic oxidation of lignin on Pt-TiO₂ under solar light illumination, *Appl. Catal. B: Environ.* 204 (2017) 296–303.
- [25] M. Chen, Y. Li, Z. Wang, Y. Gao, Y. Huang, J. Cao, W. Ho, S. Lee, Controllable synthesis of core-shell Bi@Amorphous Bi₂O₃ nanospheres with tunable optical and photocatalytic activity for NO removal, *Ind. Eng. Chem. Res.* 56 (2017) 10251–10258.
- [26] L. Yan, Z. Gu, X. Zheng, C. Zhang, X. Li, L. Zhao, Y. Zhao, Elemental bismuth–graphene heterostructures for photocatalysis from ultraviolet to infrared light, *ACS Catal.* 7 (2017) 7043–7050.
- [27] R.A. Patil, M.-K. Wei, P.H. Yeh, J.-B. Liang, W.T. Gao, J.-H. Lin, Y. Liou, Y.-R. Ma, Size-controllable synthesis of Bi/Bi₂O₃ heterojunction nanoparticles using pulsed Nd: YAG laser deposition and metal-semiconductor-heterojunction-assisted photoluminescence, *Nanoscale* 8 (2016) 3565–3571.
- [28] S. Georges, F. Goutenoire, P. Lacorre, Crystal structure of lanthanum bismuth silicate Bi₂–xLa_xSiO₅ (x~0.1), *J. Solid State Chem.* 179 (2006) 4020–4028.
- [29] D. Liu, J. Wang, M. Zhang, Y. Liu, Y. Zhu, A superior photocatalytic performance of a novel Bi₂SiO₅ flower-like microsphere via a phase junction, *Nanoscale* 6 (2014) 15222–15227.
- [30] A.K.R. Police, S. Basavaraju, D.K. Valluri, S. Machiraju, Bismuth modified porous silica preparation, characterization and photocatalytic activity evaluation for degradation of isoprotron, *J. Mater. Sci. Technol.* 29 (2013) 639–646.
- [31] J. Di, J. Xia, Y. Huang, M. Ji, W. Fan, Z. Chen, H. Li, Constructing carbon quantum dots/Bi₂SiO₅ heterostructure nanosheets with enhanced photocatalytic activity and mechanism investigation, *Chem. Eng. J.* 302 (2016) 334–343.
- [32] X. Ding, W. Ho, J. Shang, L. Zhang, Self doping promoted photocatalytic removal of no under visible light with Bi₂MoO₆: indispensable role of superoxide ions, *Appl. Catal. B: Environ.* 182 (2016) 316–325.
- [33] H. Wang, W. Zhang, X. Li, J. Li, W. Cen, Q. Li, F. Dong, Highly enhanced visible light photocatalysis and in situ FT-IR studies on Bi metal@ defective BiOCl hierarchical microspheres, *Appl. Catal. B: Environ.* 225 (2018) 218–227.
- [34] Z.F. Huang, J. Song, X. Wang, L. Pan, K. Li, X. Zhang, L. Wang, J.-J. Zou, Switching charge transfer of C₃N₄/W₁₈O₄₉ from type-II to Z-scheme by interfacial band bending for highly efficient photocatalytic hydrogen evolution, *Nano Energy* 40 (2017) 308–316.
- [35] R. Nyholm, A. Berndtsson, N. Martensson, Core level binding energies for the elements Hf to Bi (Z=72–83), *J. Phys. C: Solid State Phys.* 13 (1980) L1091.
- [36] Y. Gao, Y. Huang, Y. Li, Q. Zhang, J.J. Cao, W. Ho, S.C. Lee, Plasmonic Bi/ZnWO₄ microspheres with improved photocatalytic activity on NO removal under visible light, *ACS Sustain. Chem. Eng.* 4 (2016) 6912–6920.
- [37] M.L. Brongersma, N.J. Halas, P. Nordlander, Plasmon-induced hot carrier science and technology, *Nat. Nano* 10 (2015) 25–34.
- [38] G. Jiang, X. Li, M. Lan, T. Shen, X. Lv, F. Dong, S. Zhang, Monodisperse bismuth nanoparticles decorated graphitic carbon nitride: enhanced visible-light-response photocatalytic NO removal and reaction pathway, *Appl. Catal. B: Environ.* 205 (2017) 532–540.
- [39] S.K. Cushing, J. Li, F. Meng, T.R. Senty, S. Suri, M. Zhi, M. Li, A.D. Bristow, N. Wu, Photocatalytic activity enhanced by plasmonic resonant energy transfer from metal to semiconductor, *J. Am. Chem. Soc.* 134 (2012) 15033–15041.
- [40] L. Zhang, W. Wang, S. Sun, J. Xu, M. Shang, J. Ren, Hybrid Bi₂SiO₅ mesoporous microspheres with light response for environment decontamination, *Appl. Catal. B: Environ.* 100 (2010) 97–101.
- [41] A.B. Murphy, Band-gap determination from diffuse reflectance measurements of semiconductor films, and application to photoelectrochemical water-splitting, *Sol. Energy Mater. Sol. Cells* 91 (2007) 1326–1337.
- [42] J.A. Weil, A review of electron spin spectroscopy and its application to the study of paramagnetic defects in crystalline quartz, *Phys. Chem. Miner.* 10 (1984) 149–165.
- [43] K. Wang, Q. Li, B. Liu, B. Cheng, W. Ho, J. Yu, Sulfur-doped g-C₃N₄ with enhanced photocatalytic CO₂-reduction performance, *Appl. Catal. B: Environ.* 176–177 (2015) 44–52.
- [44] Z.-A. Lan, G. Zhang, X. Wang, A facile synthesis of Br-modified g-C₃N₄ semiconductors for photoredox water splitting, *Appl. Catal. B: Environ.* 192 (2016) 116–125.
- [45] D. Zheng, C. Pang, Y. Liu, X. Wang, Shell-engineering of hollow g-C₃N₄ nanospheres via copolymerization for photocatalytic hydrogen evolution, *Chem. Commun.* 51 (2015) 9706–9709.
- [46] J.X. Zheng, G. Ceder, T. Maxisch, W.K. Chim, W.K. Choi, First-principles study of native point defects in hafnia and zirconia, *Phys. Rev. B* 75 (2007) 104112.
- [47] H. Li, J. Shang, Z. Yang, W. Shen, Z. Ai, L. Zhang, Oxygen vacancy associated surface fenton chemistry: surface structure dependent hydroxyl radicals generation and substrate dependent reactivity, *Environ. Sci. Technol.* 51 (2017) 5685–5694.
- [48] H. Li, J. Li, Z. Ai, F. Jia, L. Zhang, Oxygen vacancy-mediated photocatalysis of BiOCl: reactivity, selectivity, and perspectives, *Angew. Chem. Int. Ed.* 57 (2018) 122–138.
- [49] G. Henkelman, A. Arnaldsson, H. Jónsson, A fast and robust algorithm for bader decomposition of charge density, *Comput. Mater. Sci.* 36 (2006) 354–360.
- [50] G. Giannona, B. Carlisi, S. Palazzo, Reaction of α,β-poly(N-hydroxyethyl)-DL-aspartamide with derivatives of carboxylic acids, *J. Polym. Sci., Part A: Polym. Chem.* 25 (1987) 2813–2818.
- [51] K. Hadjiivanov, V. Bushev, M. Kantcheva, D. Klissurski, Infrared-spectroscopy study of the species arising during NO₂ adsorption on TiO₂ (anatase), *Langmuir* 10 (1994) 464–471.
- [52] K. Hadjiivanov, V. Avreyska, D. Klissurski, T. Marinova, Surface species formed after NO adsorption and NO + O₂ coadsorption on ZrO₂ and sulfated ZrO₂: an FTIR spectroscopic study, *Langmuir* 18 (2002) 1619–1625.
- [53] K.I. Hadjiivanov, Identification of neutral and charged N x O y surface species by IR spectroscopy, *Catal. Rev.* 42 (2000) 71–144.
- [54] L. Sivachandiran, F. Thevenet, A. Rousseau, D. Bianchi, NO₂ adsorption mechanism on TiO₂: an in-situ transmission infrared spectroscopy study, *Appl. Catal. B: Environ.* 198 (2016) 411–419.
- [55] R.V. Mikhaylov, A.A. Lisachenko, B.N. Shelimov, V.B. Kazansky, G. Martra, S. Coluccia, FTIR and TPD study of the room temperature interaction of a NO–oxygen mixture and of NO₂ with titanium dioxide, *J. Phys. Chem. C* 117 (2013)

- 10345–10352.
- [56] P. Chen, F. Dong, Maoxi Ran, Jiarui Li, Synergistic photo-thermal catalytic NO purification on MnO_x/g-C₃N₄: enhanced performance and reaction mechanism, *Chin. J. Catal.* 39 (2018) 619–629.
- [57] J. Li, Z. Zhang, W. Cui, H. Wang, W. Cen, G. Johnson, G. Jiang, S. Zhang, F. Dong, The spatially oriented charge flow and photocatalysis mechanism on internal van der waals heterostructures enhanced g-C₃N₄, *ACS Catal.* 8 (2018) 8376–8385.
- [58] X. Dong, J. Li, Q. Xing, Y. Zhou, H. Huang, F. Dong, The activation of reactants and intermediates promotes the selective photocatalytic NO conversion on electron-localized Sr-intercalated g-C₃N₄, *Appl. Catal. B: Environ.* 232 (2018) 69–76.